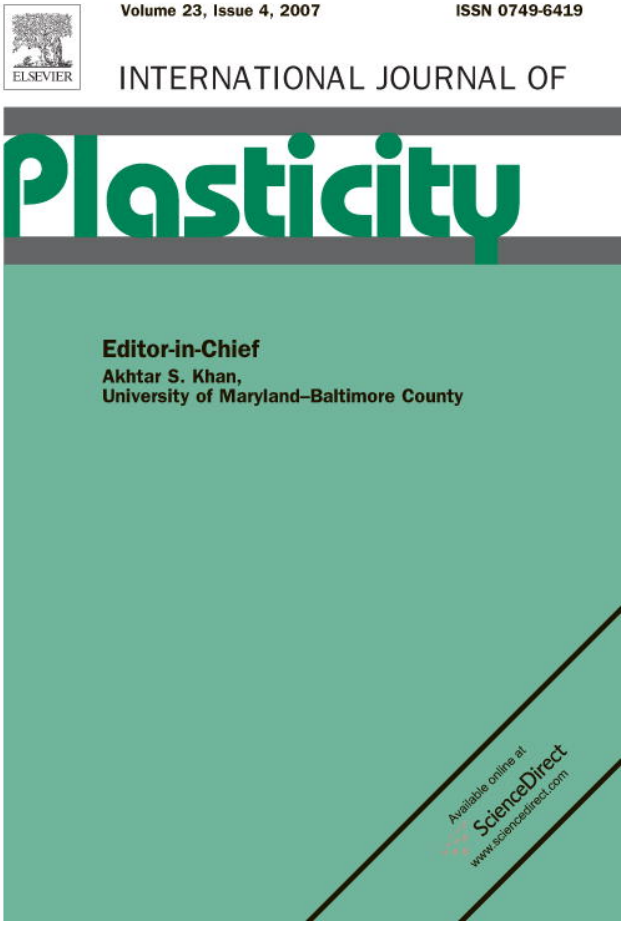

Available online at www.sciencedirect.com
ScienceDirect
International Journal of Plasticity 23 (2007) 690–710
INTERNATIONAL JOURNAL OF Plasticity
www.elsevier.com/locate/ijplas

A Finite Element approach with patch projection for strain gradient plasticity formulations

Chung-Souk Han [a,b,*], Anxin Ma [a], Franz Roters [a], Dierk Raabe [a]

[a] *Max-Planck-Institut für Eisenforschung, Max-Planck-Str. 1, 40237 Düsseldorf, Germany*
[b] *North Dakota State University, Department of Civil Engineering, Fargo, ND 58105, USA*

Received 15 April 2006
Available online 13 November 2006

Abstract

Several strain gradient plasticity formulations have been suggested in the literature to account for inherent size effects on length scales of microns and submicrons. The necessity of strain gradient related terms render the simulation with strain gradient plasticity formulation computationally very expensive because quadratic shape functions or mixed approaches in displacements and strains are usually applied. Approaches using linear shape functions have also been suggested which are, however, limited to regular meshes with equidistanced Finite Element nodes. As a result the majority of the simulations in the literature deal with plane problems at small strains. For the solution of general three dimensional problems at large strains an approach has to be found which has to be computationally affordable and robust.

For this goal a strain gradient Finite Element approach is suggested where elements with linear shape functions are applied in combination with a patch projection technique well known from error indication and adaptive mesh procedures. This approach is applied to a strain gradient crystal plasticity formulation where strain gradients are incorporated in terms of geometrically necessary dislocation densities. Simulation results of size dependent problems, including laminates in simple shear and a three dimensional contact problem, are presented and discussed to assess the performance of the suggested approach.

Keywords: A. Dislocations; B. Crystal plasticity; C. Finite elements; C. Numerical algorithms; Size dependent deformation

* Corresponding author. Present address: North Dakota State University, Department of Civil Engineering, Fargo, ND 58105, USA. Tel.: +1 701 231 5647; fax: +1 701 231 6185.
E-mail address: chung-souk.han@ndsu.edu (C.-S. Han).

0749-6419/$ - see front matter © 2006 Elsevier Ltd. All rights reserved.
doi:10.1016/j.ijplas.2006.08.003

1. Introduction

The increasing demand of components and material systems with dimensions in the micron and sub-micron range make a reliable prediction of the mechanical and material responses ever more desirable. Quite many strain gradient material formulations have been suggested for such applications in recent years which can be physically motivated by the notion of geometrically necessary dislocations providing additional hardening to the material (see, e.g., Fleck et al., 1994; Wang et al., 2004; Zaafarani et al., 2006).

The incorporation of strain gradient related terms in the material formulation requires non-conventional numerical treatments. Although the incorporation of strain gradients in Finite Element approaches with quadratic shape functions or mixed degrees of freedom in displacement and strains can be achieved on element level (Shu et al., 1999; Liebe and Steinmann, 2001; Meissonnier et al., 2001; Bittencourt et al., 2003; Soh and Wangji, 2004 and Cheong et al., 2005), these Element formulations are known to be computationally very costly and lack of robustness in large strain applications. Consequently, these formulations have been mostly applied to two dimensional problems at small strain.

For material models with micro-forces conjugated to strain gradient terms (e.g. Fleck and Hutchinson, 1997; Gao et al., 1999; Huang et al., 2000; Menzel and Steinmann, 2000; Yefimov et al., 2004; Mesarovic, 2005; Clayton et al., 2006) mixed element formulations are inevitable because of additional boundary conditions. In most applications, however, the micro-forces have arguably a quite limited impact in the interior of the material and their effect is rather limited to the close vicinity of the boundary (Huang et al., 2004). In the close neighborhood of boundaries (less than about 0.3 μm), however, the material often exhibits mechanisms which may not merely be resolved with continuum mechanics alone and is usually strongly dependent on the surface or interface characteristics (see, e.g., Han et al., 2006), which renders these micro-forces somewhat questionable.

For strain gradient models where micro-forces are not incorporated (e.g. Acharya and Bassani, 2000; Evers et al., 2002; Ohashi, 2004, 2005; Han et al., 2005a; Abu Al-Rub and Voyiadjis, 2006) higher order elements can be avoided by using the data of neighboring elements in the iteration process, as suggested in Ohashi (1997, 2004); Abu Al-Rub and Voyiadjis (2005) and Ma et al. (2006). These approaches, however, can only be used for regular meshes with equidistanced Finite Element nodes and are therefore limited in their applications. To overcome such limitations applying linear shape functions, a numerical approach is suggested in this article incorporating the patch recovery technique (Zienkiewicz and Zhu, 1987, 1992a,b) – well known from error indication and adaptive Finite Element approaches – for the determination of the strain gradients. These strain gradients from the patch recovery procedure are then incorporated into a modified Newton–Raphson iteration scheme. As material formulation a rather complex strain gradient crystal plasticity description is applied (Ma et al., 2006), formulated in terms of dislocation densities and adopting the concept of geometrically necessary dislocations. Generally, however, the suggested application of the patch projection procedure for the evaluation of strain gradient related terms can be applied to any other strain gradient or non-local material description where micro/higher order forces are not incorporated. The here applied material formulation is introduced in the next section followed by the suggested numerical approach incorporating the patch recovery procedure. Two numerical examples are presented and discussed to illustrate the performance of the suggested approach.

2. Dislocation based non-local crystal plasticity model

The applied material formulation is only briefly summarized in the following, the detailed description and derivation is rather lengthy and omitted for brevity. More details can be found in Ma and Roters (2004); Ma et al. (2006). For clarity of the notation we recall the standard multiplicative decomposition of deformation gradient (1) where the lattice rotation $\mathbf{R}_{\star}$ is included in $\mathbf{F}_e$ and plastic slip is represented by $\mathbf{F}_p$. In the intermediate configuration $\widetilde{\mathscr{B}}$, the plastic velocity gradient can be expressed by (3), where $\dot{\gamma}^\alpha$ denotes the plastic shearing rate, $\tilde{\mathbf{d}}^\alpha$ the slip direction, and $\tilde{\mathbf{n}}^\alpha$ the slip plane normal of slip system α in $\widetilde{\mathscr{B}}$ with $|\tilde{\mathbf{d}}^\alpha| = |\tilde{\mathbf{n}}^\alpha| = 1$ and $\tilde{\mathbf{d}}^\alpha \cdot \tilde{\mathbf{n}}^\alpha = 0$. Further important equations are listed in Table 1, where $\boldsymbol{\tau}$ denotes the Kirchhoff stress tensor and $\widetilde{\mathbb{K}}_e$ the elasticity tensor in $\widetilde{\mathscr{B}}$.

The material model is formulated in terms for evolution equations for different dislocation densities resolved to individual slip systems (see Ma et al., 2006; Ma and Roters, 2004; Roters, 2003). The concept of dividing the dislocation density into statistically stored ρ_{SS} and geometrically necessary dislocation densities ρ_{GN} is applied (Fleck et al., 1994), where different dislocation density classes are distinguished in the hardening description related to each individual slip system (Arsenlis and Parks, 1999; Evers et al., 2002; Ma et al., 2006). The flow rule and hardening description for the dislocation density based material formulation are given in Table 2, where the interaction coefficients, $\chi_{\alpha\beta}$, in Eqs. (13 and 14), can be found in Arsenlis and Parks (1999). The evolution equations for the statistical stored ρ^α_{SS} and geometrically necessary dislocation densities ρ^α_{GN} associated to a slip system α are given in Tables 3 and 4, respectively.

The material formulation incorporates rate and temperature dependence and necessitates the material parameters $c_1, \ldots, c_8$ and physical constants of the material, i.e. Boltzmann constant K_B, Burgers vector length b, shear modulus G, Poisson's ratio ν, and the effective activation energy for dislocation slip Q_{slip} and climb Q_{bulk}, respectively. As Q_{slip} and Q_{bulk} are very difficult to determine, both parameters can be considered to actually be material parameters. The temperature of the material is denoted by θ. It should be carefully noted that with the gradients in $\dot{\gamma}^\alpha \mathbf{F}_p^T$ in Eqs. (20)–(22) of Table 4 the material formulation renders to be non-local. For clarity, the rotation or Curl of a tensor field applied in

Table 1
Kinematic relations in the intermediate configuration $\widetilde{\mathscr{B}}$

Deformation gradient : $\mathbf{F} = \mathbf{F}_e\mathbf{F}_p$	(1)
Velocity gradient : $\mathbf{l} = \mathbf{l}_e + \mathbf{F}_e\widetilde{\mathbf{L}}_p\mathbf{F}_e^{-1}$ with $\mathbf{l}_e = \dot{\mathbf{F}}_e\mathbf{F}_e^{-1}$ and $\widetilde{\mathbf{L}}_p = \dot{\mathbf{F}}_p\mathbf{F}_p^{-1}$	(2)
Plastic velocity gradient : $\widetilde{\mathbf{L}}_p = \sum_\alpha \dot{\gamma}^\alpha \tilde{\mathbf{d}}^\alpha \otimes \tilde{\mathbf{n}}^\alpha$	(3)
Lagrangian strain tensor : $\widetilde{\mathbf{E}} = \frac{1}{2}(\mathbf{F}_e^T\mathbf{F}_e - \mathbf{F}_p^{-T}\mathbf{F}_p^{-1}) = \widetilde{\mathbf{E}}_e + \widetilde{\mathbf{E}}_p$	(4)
$\widetilde{\mathbf{E}}_e = \frac{1}{2}(\mathbf{F}_e^T\mathbf{F}_e - \mathbf{1})$ and $\widetilde{\mathbf{E}}_p = \frac{1}{2}(\mathbf{1} - \mathbf{F}_p^{-T}\mathbf{F}_p^{-1})$	(5)
2nd Piola–Kirchhoff stress : $\widetilde{\mathbf{S}} = \mathbf{F}_e^{-1}\boldsymbol{\tau}\mathbf{F}_e^{-T}$	(6)
Elastic relation : $\widetilde{\mathbf{S}} = \widetilde{\mathbb{K}}_e\widetilde{\mathbf{E}}_e$	(7)
Mandel stress : $\widetilde{\mathbf{P}} = (\mathbf{1} + 2\widetilde{\mathbf{E}}_e)\widetilde{\mathbf{S}} = \widetilde{\mathbf{C}}_e\widetilde{\mathbf{S}}$	(8)
Resolved shear stress : $\tau^\alpha = \widetilde{\mathbf{P}} \cdot (\tilde{\mathbf{d}}^\alpha \otimes \tilde{\mathbf{n}}^\alpha)$ where $\mathbf{A} \cdot \mathbf{B} = \sum_{ij} A_{ij}B_{ij}$	(9)

Table 2
Dislocation density based crystal plasticity model

$$\text{Flow rule}: \ \dot{\gamma}^{\alpha} = \dot{\gamma}_0 \sinh\left[-\frac{Q_{\text{slip}}}{\mathrm{K_B}\theta}\left(1-\frac{|\tau^{\alpha}|-\tau^{\alpha}_{\text{pass}}}{\tau^{\alpha}_{\text{cut}}}\right)\right]\text{sign}(\tau^{\alpha}) \tag{10}$$

$$\text{Reference shear rate}: \ \dot{\gamma}_0 = \frac{\mathrm{K_B}\theta v_0}{c_1 c_3 G b^2}\sqrt{\rho^{\alpha}_{\mathrm{P}}} \tag{11}$$

$$\text{Passing stress}: \ \tau^{\alpha}_{\text{pass}} = c_1 G b\sqrt{\rho^{\alpha}_{\mathrm{P}}}, \quad \text{Cutting stress}: \ \tau^{\alpha}_{\text{cut}} = \frac{Q_{\text{slip}}}{c_2 c_3 b^2}\sqrt{\rho^{\alpha}_{\mathrm{F}}} \tag{12}$$

$$\begin{aligned}\text{Forest dislocation with } \tilde{\mathbf{t}}_{\alpha} = \tilde{\mathbf{d}}_{\alpha}\times\tilde{\mathbf{n}}_{\alpha}: \ \rho^{\alpha}_{\mathrm{F}} = \sum_{\beta=1}^{N}\chi_{\alpha\beta}[&\rho^{\beta}_{\mathrm{SS}}\,|\cos(\tilde{\mathbf{n}}_{\alpha},\tilde{\mathbf{t}}_{\beta})| \\ &+ |\rho^{\beta}_{\mathrm{GN}s}\cos(\tilde{\mathbf{n}}_{\alpha},\tilde{\mathbf{d}}_{\beta})| + |\rho^{\beta}_{\mathrm{GN}et}\cos(\tilde{\mathbf{n}}_{\alpha},\tilde{\mathbf{t}}_{\beta})| \\ &+ |\rho^{\beta}_{\mathrm{GN}en}\cos(\tilde{\mathbf{n}}_{\alpha},\tilde{\mathbf{n}}_{\beta})|]\end{aligned} \tag{13}$$

$$\begin{aligned}\text{Parallel dislocation}: \ \rho^{\alpha}_{\mathrm{P}} = \sum_{\beta=1}^{N}\chi_{\alpha\beta}[&\rho^{\beta}_{\mathrm{SS}}|\sin(\tilde{\mathbf{n}}_{\alpha},\tilde{\mathbf{t}}_{\beta})| + |\rho^{\beta}_{\mathrm{GN}s}\sin(\tilde{\mathbf{n}}_{\alpha},\tilde{\mathbf{d}}_{\beta})| \\ &+ |\rho^{\beta}_{\mathrm{GN}et}\sin(\tilde{\mathbf{n}}_{\alpha},\tilde{\mathbf{t}}_{\beta})| + |\rho^{\beta}_{\mathrm{GN}en}\sin(\tilde{\mathbf{n}}_{\alpha},\tilde{\mathbf{n}}_{\beta})|]\end{aligned} \tag{14}$$

Table 3
Evolution of the statistically stored dislocation density

$$\text{Statistical stored dislocation density}: \ \dot{\rho}^{\alpha}_{\mathrm{SS}} = (\dot{\rho}^{\alpha+}_{\mathrm{SS}})_{\text{locks}} + (\dot{\rho}^{\alpha+}_{\mathrm{SS}})_{\text{dipole}} + (\dot{\rho}^{\alpha-}_{\mathrm{SS}})_{\text{athermal}} + (\dot{\rho}^{\alpha-}_{\mathrm{SS}})_{\text{thermal}}$$

$$\text{Lock formation}: \ (\dot{\rho}^{\alpha+}_{\mathrm{SS}})_{\text{locks}} = c_4\sqrt{\rho^{\alpha}_{\mathrm{F}}}\dot{\gamma}^{\alpha} \tag{15}$$

$$\text{Dipole formation}: \ (\dot{\rho}^{\alpha+}_{\mathrm{SS}})_{\text{dipole}} = c_6 d^{\alpha}_{\text{dipole}}\rho^{\alpha}_{\mathrm{M}}\dot{\gamma}^{\alpha} \tag{16}$$

$$\text{where } d^{\alpha}_{\text{dipole}} = \frac{\sqrt{3}Gb}{16\pi(1-\nu)}(|\tau^{\alpha}|-\tau^{\alpha}_{\text{pass}})^{-1} \text{ and } \rho^{\alpha}_{\mathrm{M}} \approx \frac{2\mathrm{K_B}\theta}{c_1 c_2 c_3 G b^3}\sqrt{\rho^{\alpha}_{\mathrm{P}}\rho^{\alpha}_{\mathrm{F}}}$$

$$\text{Athermal annihilation}: \ (\dot{\rho}^{\alpha-}_{\mathrm{SS}})_{\text{athermal}} = -c_5\rho^{\alpha}_{\mathrm{SS}}\dot{\gamma}^{\alpha} \tag{17}$$

$$\text{Thermal annihilation}: \ (\dot{\rho}^{\alpha-}_{\mathrm{SS}})_{\text{thermal}} = -c_7\exp\left(-\frac{Q_{\text{bulk}}}{\mathrm{K_B}\theta}\right)\frac{|\tau^{\alpha}|}{\mathrm{K_B}\theta}(\rho^{\alpha}_{\mathrm{SS}})^2(\dot{\gamma})^{c_8} \tag{18}$$

Table 4
Evolution of geometrically necessary dislocation density

Geometrically necessary dislocation density :

$$(\dot{\rho}^{\alpha}_{\mathrm{GN}})^2 = (\dot{\rho}^{\alpha}_{\mathrm{GN}s})^2 + (\dot{\rho}^{\alpha}_{\mathrm{GN}et})^2 + (\dot{\rho}^{\alpha}_{\mathrm{GN}en})^2 \tag{19}$$

$$\dot{\rho}^{\alpha}_{\mathrm{GN}s} = \frac{1}{b}(\nabla_X \times (\dot{\gamma}^{\alpha}\mathbf{F}^{\mathrm{T}}_{\mathrm{P}})\tilde{\mathbf{n}}_{\alpha})\cdot\tilde{\mathbf{d}}^{\alpha} \tag{20}$$

$$\dot{\rho}^{\alpha}_{\mathrm{GN}et} = \frac{1}{b}(\nabla_X \times (\dot{\gamma}^{\alpha}\mathbf{F}^{\mathrm{T}}_{\mathrm{P}})\tilde{\mathbf{n}}_{\alpha})\cdot\tilde{\mathbf{t}}^{\alpha} \tag{21}$$

$$\dot{\rho}^{\alpha}_{\mathrm{GN}en} = \frac{1}{b}(\nabla_X \times (\dot{\gamma}^{\alpha}\mathbf{F}^{\mathrm{T}}_{\mathrm{P}})\tilde{\mathbf{n}}_{\alpha})\cdot\tilde{\mathbf{n}}^{\alpha} \tag{22}$$

Table 4 is given by $\nabla_X \times \mathbf{T} = \mathrm{Curl}\mathbf{T} = \epsilon_{irs}\frac{\partial T_{js}}{\partial X_r}\mathbf{e}_i \otimes \mathbf{e}_j$ where ϵ_{irs} denotes the permutation symbol and $\mathbf{e}_i$ are the orthonormal coordinate vectors to X_i in the reference configuration $\mathscr{B}_0$. It might be noteworthy that the expressions (20)–(23) are derived via

$\boldsymbol{\Lambda} = -\frac{1}{b}(\nabla_X \times \mathbf{F}_\mathrm{p}^\mathrm{T})^\mathrm{T}$ (Nye, 1953) yielding $\dot{\boldsymbol{\Lambda}} = \sum_\alpha -\frac{1}{b}\tilde{\mathbf{d}}^\alpha \otimes [\nabla_X \times (\dot{\gamma}^\alpha \mathbf{F}_\mathrm{P}^\mathrm{T})\tilde{\mathbf{n}}^\alpha] = \sum_\alpha \dot{\boldsymbol{\Lambda}}^\alpha$ where $\dot{\boldsymbol{\Lambda}}^\alpha = -\dot{\rho}^\alpha_{\mathrm{GN}s}\tilde{\mathbf{d}}^\alpha \otimes \mathbf{d}^\alpha - \dot{\rho}^\alpha_{\mathrm{GN}en}\tilde{\mathbf{d}}^\alpha \otimes \tilde{\mathbf{t}}^\alpha - \dot{\rho}^\alpha_{\mathrm{GN}en}\tilde{\mathbf{d}}^\alpha \otimes \tilde{\mathbf{n}}^\alpha$ (Dai and Parks, 1997) whose norm in turn is equivalent to (19).

3. Stress integration procedure

The algorithmic treatment of the evolution equations given in the previous sections is described in the following. As starting point all variables at time step t_n are assumed to be known and the current time is given with t_{n+1}. In what follows, however, all variables without subscript are evaluated at t_{n+1}. Within the implicit Finite Element approach a stress tensor and tangent moduli have to be provided and necessary history variables updated. The plastic deformation gradient can be written as $\mathbf{F}_\mathrm{p} = \exp(\Delta t \widetilde{\mathbf{L}}_\mathrm{p})\mathbf{F}_\mathrm{p}^n$, which is approximated here by $\mathbf{F}_\mathrm{p} \approx (\mathbf{1} + \sum_\alpha \Delta\gamma^\alpha \tilde{\mathbf{d}}^\alpha \otimes \tilde{\mathbf{n}}^\alpha)\mathbf{F}_\mathrm{p}^n$. Assuming no plastic deformation, the trial value for the elastic deformation gradient is obtained as $\mathbf{F}_\mathrm{e}^* = \mathbf{F}(\mathbf{F}_\mathrm{p}^n)^{-1}$ and, correspondingly, $\widetilde{\mathbf{C}}_\mathrm{e}^* = \mathbf{F}_\mathrm{e}^{*\mathrm{T}}\mathbf{F}_\mathrm{e}^*$. With the trial stresses $\widetilde{\mathbf{S}}^* = \widetilde{\mathbb{K}}_\mathrm{e}\frac{1}{2}(\widetilde{\mathbf{C}}_\mathrm{e}^* - \mathbf{1})$ and neglecting quadratic and higher terms in $\Delta\gamma^\alpha$ the stresses are obtained as

$$\widetilde{\mathbf{S}} = \widetilde{\mathbf{S}}^* - \widetilde{\mathbb{K}}_\mathrm{e}(\widetilde{\mathbf{C}}_\mathrm{e}^* \sum_\alpha \Delta\gamma^\alpha \tilde{\mathbf{d}}^\alpha \otimes \tilde{\mathbf{n}}^\alpha)_S \tag{23}$$

where $(.)_S = \frac{1}{2}((.) + (.)^\mathrm{T})$ and $\widetilde{\mathbb{K}}_\mathrm{e}$ contains the elastic moduli. Because elastic strains are usually small in metal plasticity the Mandel stress tensor $\widetilde{\mathbf{P}}$ in Eq. (8) is as usual approximated by $\widetilde{\mathbf{S}}$ (see, e.g., Kalidindi and Anand, 1992). Assuming $\mathbf{F}$ and $\mathbf{F}_\mathrm{p}^n$ to be given, the slip increments $\Delta\gamma^\alpha$, $\alpha = 1, \ldots, n_\mathrm{slip}$ have therefore to be determined for $\widetilde{\mathbf{S}}$. With (10) the increments in slip have in turn the dependence on stresses via (9), i.e.

$$\Delta\gamma^\alpha = \Delta\gamma^\alpha(\tau^\alpha, \rho^\alpha_\mathrm{SS}, \rho^\alpha_\mathrm{GN}, \alpha = 1, \ldots, n_\mathrm{slip}) \tag{24}$$

$$\text{where } \rho^\alpha_\mathrm{SS} = \rho^{\alpha^n}_\mathrm{SS} + \Delta\rho^\alpha_\mathrm{SS} \quad \text{with } \Delta\rho^\alpha_\mathrm{SS} = \Delta\rho^\alpha_\mathrm{SS}(\widetilde{\mathbf{S}}, \rho^\alpha_\mathrm{SS}, \rho^\alpha_\mathrm{GN}, \alpha = 1, \ldots, n_\mathrm{slip}) \tag{25}$$

$$\text{and} \quad \rho^\alpha_\mathrm{GN} = \rho^{\alpha^n}_\mathrm{GN} + \Delta\rho^\alpha_\mathrm{GN} \quad \text{with } \Delta\rho^\alpha_\mathrm{GN} = \Delta\rho^\alpha_\mathrm{GN}(\nabla_X \times (\Delta\gamma^\alpha \mathbf{F}_\mathrm{p}^\mathrm{T}), \alpha = 1, \ldots, n_\mathrm{slip}) \tag{26}$$

and these Eqs. (23)–(26) have to be solved simultaneously. This is achieved by a Newton iteration scheme.

With (26) gradients of

$$\boldsymbol{\Omega}^\alpha = \Delta\gamma^\alpha \mathbf{F}_\mathrm{p}^\mathrm{T} \tag{27}$$

have to be provided. Assuming these gradients to be given the stresses in the intermediate configuration, $\widetilde{\mathbf{S}}$, can be calculated according to the elastic predictor–plastic corrector concept in crystal plasticity (e.g. Kalidindi and Anand, 1992; Cuitino and Ortiz, 1992; Miehe and Schröder, 2001; Han et al., 2004). While the derivation is far from trivial it is omitted here for brevity and referred to Ma et al. (2006) for more details.

As with linear shape functions strain-type terms are essentially constant, the gradients in $\boldsymbol{\Omega}^\alpha$ as required in (26) would necessitate higher order Finite Elements, i.e. quadratic shape functions (e.g. Meissonnier et al., 2001) or mixed Finite Elements where strain-like terms are nodal variables (e.g. Shu et al., 1999). Both options are computationally very costly and in view of, e.g., FCC crystals with 12 slip systems and corresponding 12 shear strains γ^α at least mixed approaches seem to be far too costly for general 3D applications.

As low order Finite Elements shall be applied in this approach, information of neighboring elements has to be incorporated because linear shape functions – as mentioned above – basically yield a constant strain field within an element. To obtain a continuous field in $\mathbf{\Omega}^{\alpha}$ which can then deliver the gradients required for (26) it is here suggested to project the element values of $\mathbf{\Omega}^{\alpha}$ at the integration points to the nodes by the patch projection procedure which in turn can be interpolated and differentiated with the aid of conventional FE shape functions.

3.1. Patch recovery and strain gradients

The suggested projection technique (Zienkiewicz and Zhu, 1987, 1992a) has found broad application in the error indication and adaptive Finite Element applications for linear (e.g. Zienkiewicz and Zhu, 1992a) and nonlinear problems (e.g. Han and Wriggers, 2000). For the convenience of the reader this approach is outlined in the following.

For the projection from the integration points to nodal points a patch is chosen, which includes all elements containing node I. A linear interpolation of coefficients Ω^{α}_{mn} of tensor $\mathbf{\Omega}^{\alpha}$ shall be obtained which is expressed here by

$$\Omega^{\alpha}_{mn} = \mathbf{p}^{\mathrm{T}}\mathbf{y} \tag{28}$$

with $\mathbf{p} = [1, x_1, x_2, x_3, x_1x_2, x_1x_3, x_2x_3, x_1x_2x_3]^{\mathrm{T}}$ and $\mathbf{y} = [y_1, y_2, y_3, y_4, y_5, y_6, y_7, y_8]^{\mathrm{T}}$. The goal is to determine the coefficients of $\mathbf{y}$ in such a way that the square in the difference between the linear interpolation and the integration points is minimized by a least square fit of a patch including all elements containing node I, see Fig. 1 for the two dimensional case. With i as an index for all integration points of this patch the minimization can be stated as

$$\sum_i (\mathbf{p}_i^{\mathrm{T}}\mathbf{y} - \Omega^{\alpha}_{mn_i})^2 \rightarrow \mathrm{Min} \tag{29}$$

The first derivative of this equation yields the necessary condition which is applied to determine the coefficients contained in $\mathbf{y}$, i.e. the projection is performed via

$$\mathbf{A}\mathbf{y} = \mathbf{b}, \quad \text{where } \mathbf{A} = \sum_i \mathbf{p}_i\mathbf{p}_i^{\mathrm{T}} \text{ and } \mathbf{b} = \sum_i \Omega^{\alpha}_{mn_i}\mathbf{p}_i \tag{30}$$

with $\mathbf{p}_i = \mathbf{p}(\mathbf{X}_i)$, where $\mathbf{X}_i$ are the coordinates of the integration points. To ensure a good condition and to avoid singularities of the matrix $\mathbf{A}$ a local coordinate system with its ori-

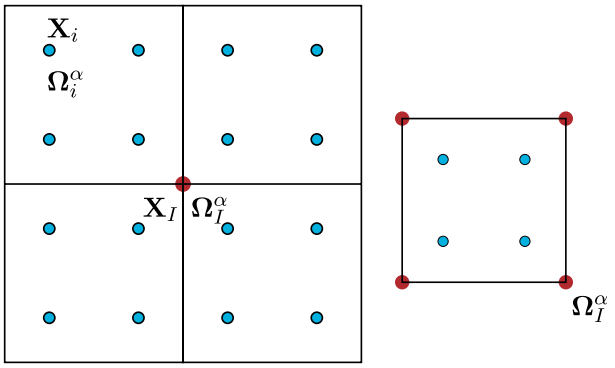

Fig. 1. Projection from integration points to nodal points and interpolation from nodal points to integration points (2-dimensional scheme for illustration).

gin in the node I is chosen with the coordinates normalized over a characteristic length of an Finite Element of the patch. The projected value at node I is then obtained with

$$\Omega^{\alpha}_{mn_I} = \Omega^{\alpha}_{mn}(\mathbf{X}_I) = \mathbf{p}^{\mathrm{T}}(\mathbf{X}_I)\mathbf{y} \tag{31}$$

and this procedure has to be repeated for $m,n = 1,2,3$ and all Finite Element nodes.

With Ω^{α}_{mn} now available on all nodes an continuous field in $\mathbf{\Omega}^{\alpha}$ is obtained via $\mathbf{\Omega}^{\alpha} = \sum_I N_I(\mathbf{X})\mathbf{\Omega}^{\alpha}_I$ with the usual shape functions N_I. The tensor $\mathbf{\Omega}^{\alpha}$ is differentiable in the interior of the elements and its Curl can be determined as

$$\nabla_X \times \mathbf{\Omega}^{\alpha}(\mathbf{X}) = \sum_I \epsilon_{nrs} \frac{\partial N_I(\mathbf{X})}{\partial X_r} \Omega^{\alpha}_{I_{js}} \mathbf{e}_n \otimes \mathbf{e}_j. \tag{32}$$

At boundaries only a few elements are generally associated with a node which does not provide adequate information for the linear least square fit suggested above. In this case (as suggested in Zienkiewicz and Zhu, 1987) another node is chosen to define the patch for the node on which the $\mathbf{\Omega}^{\alpha}$ values are projected – namely the closest internal node I_{patch}, see Fig. 2. Although it is known that this approach does not yield the same quality as the projected values at the internal nodes, other more complex projection procedures, as suggested in Wiberg et al. (1994), and Boroomand and Zienkiewicz (1997), for common boundaries and in Rieger and Wriggers (2004), and Han and Wriggers (2002) for contact boundaries can not be applied for the projection of plastic strain as these procedures deduce their projected values from improved traction/contact force at the boundaries.

It should also be remarked that better projected values may be obtained by applying the superconvergent projection technique (Zienkiewicz and Zhu, 1992a) where the support points for the least square fit are not the integration points but the mid points of the elements, as indicated in Fig. 3. These points are known to have the superconvergent properties in linear elasticity. For this approach the stress integration would have to be additionally evaluated at these points due to the history dependence of the material procedure. While the patch projection techniques has been derived for linear elastic problems it has been also successfully applied to elasto-plastic problems, see, e.g., Boroomand and Zienkiewicz (1999) and Han and Wriggers (2000). It may be worth noting that particularly if superconvergent points are used the origin of the axes applied in the patch recovery pro-

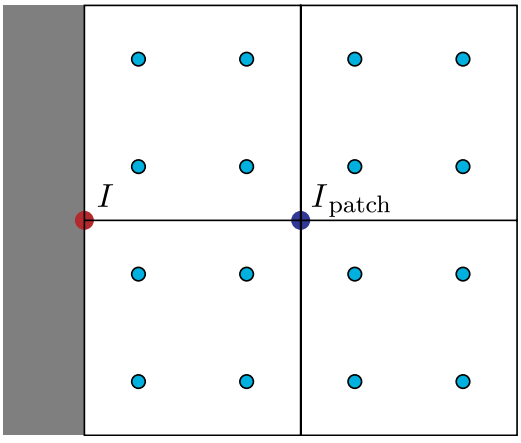

Fig. 2. Projection for nodes at boundaries.

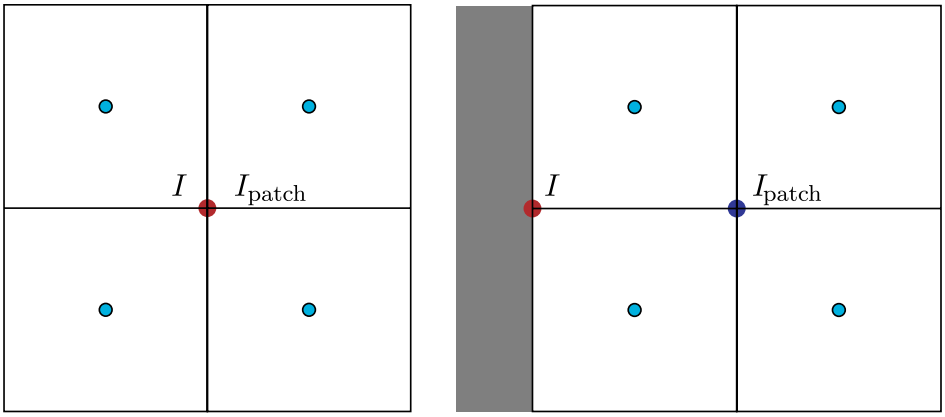

Fig. 3. Projection for using superconvergent points.

cedure should be set to the coordinates of I_{patch} and the orientation of these axes should be chosen in such a way that at least one axis is parallel to an edge of an element to avoid ill conditioned **A** matrices in (30).

For regular meshes in the interior the above suggested approach may yield similar values as those suggested in Abu Al-Rub and Voyiadjis (2005) and Ma et al. (2006). These methods are, however, restricted to regular equidistant meshes while the patch recovery approach can also be applied to not-regular meshes, where for instance the orientation and size of the elements can change. The use of irregular meshes has its limitations because strongly irregular elements, as discussed in the error indication and adaptive meshing literature, see, e.g., Zienkiewicz and Zhu (1992a); Boroomand and Zienkiewicz (1997), can yield excessive unphysical stresses and strains which in turn would also make the projected values and their strain gradients not reliable. The quality of the mesh is therefore an important issue for this approach. As this approach is also applicable to triangles and tetrahedrons and mixed meshes with both tetrahedrons and brick elements ill-shaped elements could be to a certain extend avoided. Further advantages of the suggested procedure applying the patch recovery technique lie in the simplicity of the procedure and their thoroughly discussed behavior and characteristics in the literature, e.g. modifications of the outlined approach for brick elements to triangle and tetrahedron elements or mixed discretizations can be found in Zienkiewicz and Zhu (1992a).

3.2. Overall iteration procedure

The patch projection procedure has to be incorporated into the overall iteration within the Newton–Raphson scheme for each load step. This is implemented by an additional iteration loop (B) for the increments in the geometrically necessary dislocation densities illustrated in Table 5. To clarify the terms used in Table 5 the applied Newton–Raphson iteration is briefly recalled. The weak form of equilibrium for static problems can be stated as $q(\mathbf{u},\delta\mathbf{u}) = \int_{\mathscr{B}} \mathbf{S}\cdot\delta\mathbf{E}\,\mathrm{d}V - p(\mathbf{u},\delta\mathbf{u})$ with the load terms contained in p, i.e. $p(\mathbf{u},\delta\mathbf{u}) = \int_{\mathscr{B}} \rho_0\bar{\mathbf{b}}\cdot\delta\mathbf{u}\,\mathrm{d}V - \int_{\partial\mathscr{B}} \bar{\mathbf{t}}\cdot\delta\mathbf{u}\,\mathrm{d}A$. The FEM discretization yields (see, e.g., Wriggers, 2001)

$$\int_{\mathscr{B}} \mathbf{S}\cdot\delta\mathbf{E}\,\mathrm{d}V \approx \bigcup_{e=1}^{n_e}\sum_{I=1}^{n_I} \delta\mathbf{u}_I^{\mathrm{T}} \int_{V_e} \mathbf{B}_I^{\mathrm{T}}\mathbf{S}_e\,\mathrm{d}V = \bigcup_{e=1}^{n_e}\sum_{I=1}^{n_I} \delta\mathbf{u}_I^{\mathrm{T}}\mathbf{R}_I(\mathbf{u}_e) \tag{33}$$

where $\mathbf{R}_I(\mathbf{u}_e) = \int_{V_e} \mathbf{B}_I^{\mathrm{T}}\mathbf{S}_e\,\mathrm{d}V$. With $\mathbf{R}(\mathbf{u}) = \bigcup_{e=1}^{n_e}\sum_{I=1}^{n_I}\mathbf{R}_I(\mathbf{u}_e)$ we obtain

Table 5
Overall, non-local iteration procedure

Set $\mathbf{u}_0 = \mathbf{u}_k$, $\mathbf{F}_{\mathrm{p}_0} = \mathbf{F}_{\mathrm{p}_k}$, $\rho^\alpha_{\mathrm{SS}_0} = \rho^\alpha_{\mathrm{SS}_k}$, $\rho^\alpha_{\mathrm{GN}_0} = \rho^\alpha_{\mathrm{GN}_k}$
(A) Load steps $k = 0, 1, \ldots, k_{\max}$
  (B) Iteration from $i = 0, 1, \ldots, i_{\max}$
    (I) Determine $\boldsymbol{\tau}^\alpha_i$, $\mathbf{F}_{\mathrm{p}_i}$, and $\rho^\alpha_{\mathrm{SS}_i}$ with $\rho^\alpha_{\mathrm{GN}} = \rho^\alpha_{\mathrm{GN}_k}$ via local iteration at integration points
    (II) Determine $\mathbf{Q}(\mathbf{u}_i, \lambda_k)$, $\mathbf{K}_{\mathrm{T}}(\mathbf{u}_i)$ and solve $\mathbf{K}_{\mathrm{T}}(\mathbf{u}_i)\Delta\mathbf{u} = -\mathbf{Q}(\mathbf{u}_i, \lambda_k)$
    (III) $\mathbf{u}_{i+1} = \mathbf{u}_i + \Delta\mathbf{u}_{i+1}$
    (IV) Determine $\boldsymbol{\Omega}^\alpha$ on all nodes via patch projection Eqs. (30)–(32) and
      calculate $\rho^\alpha_{\mathrm{GN}_{k+1}} = \rho^\alpha_{\mathrm{GN}_0} + \Delta\rho^\alpha_{\mathrm{GN}_k}$ via Eqs. (19)–(22) on all integration points
    (V) Check convergence
      • if $|\rho^\alpha_{\mathrm{GN}_i} - \rho^\alpha_{\mathrm{GN}_{i+1}}| \leqslant tol$ $\forall$ integration points and $|\mathbf{Q}(\mathbf{u}_{i+1})| \leqslant tol$
        then
        $\rightarrow \mathbf{u}_{k+1} = \mathbf{u}_{i+1}$,
        $\rightarrow \mathbf{F}_{\mathrm{p}_{k+1}} = \mathbf{F}_{\mathrm{p}_{i+1}}$, $\rho^\alpha_{\mathrm{SS}_{k+1}} = \rho^\alpha_{\mathrm{SS}_{i+1}}$, $\rho^\alpha_{\mathrm{GN}_{k+1}} = \rho^\alpha_{\mathrm{GN}_{i+1}}$,
        $\rightarrow k = k + 1$, and
        $\rightarrow$ goto (A)
      • else $i = i + 1$ and goto (I)

$$\mathbf{Q}(\mathbf{u}, \lambda) = \mathbf{R}(\mathbf{u}) - \lambda\mathbf{P} = \mathbf{0} \tag{34}$$

with a load parameter λ representing the prescribed loads. Assuming that the loads are independent of the displacements, the linearization of (34) at $\mathbf{u}_k$ yields the tangential stiffness matrix $\mathbf{K}_{\mathrm{T}}$ via $\mathbf{Q}(\mathbf{u}_k + \Delta\mathbf{u}, \lambda_k) \approx \mathbf{Q}(\mathbf{u}_k, \lambda_k) + D\mathbf{Q}(\mathbf{u}_k, \lambda_k)\Delta\mathbf{u} = \mathbf{Q}(\mathbf{u}_k, \lambda_k) + \mathbf{K}_{\mathrm{T}}\Delta\mathbf{u}$.

For each iteration k for ρ_{GN_k} the integration procedure is performed for fixed ρ_{GN_k}. If the convergence criteria in step (V) are fulfilled the state variables are updated and the next load step is calculated. For simple problems as presented in Section 4.1 the loop for the determination of ρ_{GN} required only a few iterations with reasonable tolerances, *tol*, in step (V).

4. Numerical examples

Two problems will be discussed in the following to assess the suggested approach. For both problems aluminum is chosen as material with initially homogeneously distributed dislocation densities. The initial dislocation density for every slip system is set to be $\rho^\alpha = 1.5 \times 10^{11}\ \frac{1}{\mathrm{m}^2}$ for all sip systems, the temperature to 293 K, the attack frequency to $\nu_0 = 1 \times 10^{10}\ \frac{1}{\mathrm{s}}$, and Burgers vector length to $b = 2.86 \times 10^{-10}$ m. Other material parameters are given in Table 6.

4.1. Simple shear of a laminar layer

In the first example a single crystal aluminum layer between rigid solids deformed in shear and plane strain is considered, as illustrated in Fig. 4. This simple example is chosen

Table 6
Material parameters applied in the simulations

$Q_{\mathrm{edge}} = 3.0 \times 10^{-19}$ J	$c_1 = 0.1$	$c_3 = 0.4$	$c_5 = 10^{-3}$	$c_7 = 10.0$
$Q_{\mathrm{bulk}} = 2.4 \times 10^{-19}$ J	$c_2 = 2.0$	$c_4 = 25.0/\mathrm{m}$	$c_6 = 10.0$	$c_8 = 0.3$

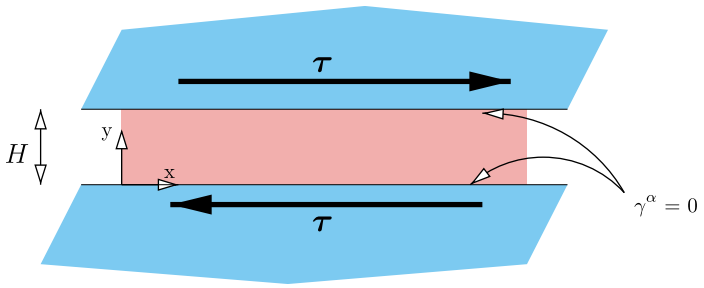

Fig. 4. A layer in shear deformation between two rigid materials.

to study the convergence behavior with respect to the element density of the Finite Element discretization. A similar problem has also been applied in Niordson and Hutchinson (2003) for a phenomenological strain gradient plasticity description without taking specific slip planes into account. The structure has been calculated for different heights H where the ratio between the height and the length L of the layer is kept constant at $H/L = 1/10$. Each of the simulations are divided into 200 time steps to result in a total shear of 0.01 in a time frame of 100 second. The (1 0 0) orientation has been rotated by an angle of 30° while the (0 0 1) remains parallel to the z-axis (which is the out-of-plane axes). As in Han et al. (2005b), in the interface between the rigid material and the single crystal it is assumed that no plastic deformation takes place, thus $\dot{\gamma}^\alpha = 0$ for all slip systems α.

The distribution of the total statistically stored and total geometrically necessary dislocation density over a structure with $H = 0.0125$ mm is illustrated in Figs. 5 and 6, respectively. Therein and in the following, the initial dislocation density is not contained in ρ_{SS} and ρ_{GN}. As the statistically stored dislocations increase with the plastic deformation their densities are higher in the middle of the layer (Fig. 5) while the opposite case is present for the densities of geometrically necessary dislocations (Fig. 6). Because the left and right boundary is free boundary effects are present which however do not seem to affect the middle of the layer whose total densities in statistically stored and geometrically necessary dislocations is shown in Fig. 7 for a mesh with 20 equidistant elements through the height H.

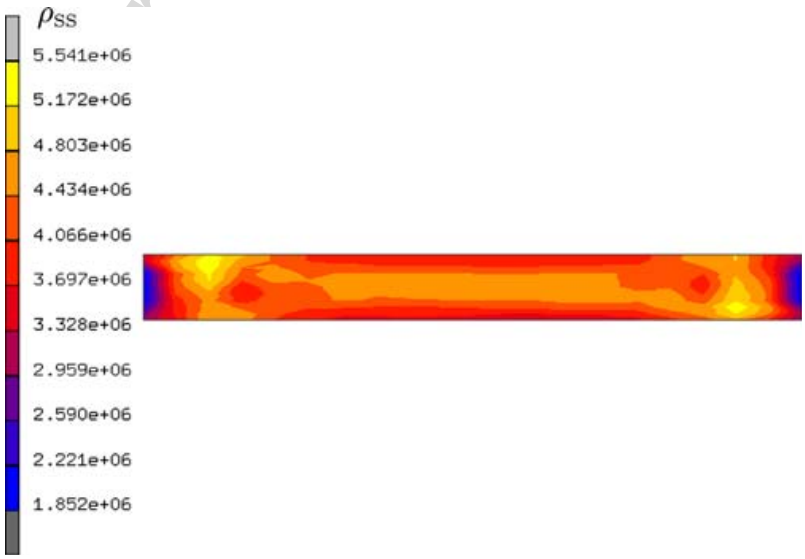

Fig. 5. Distribution of total statistically stored dislocation densities ρ_{SS} in 1/mm^2.

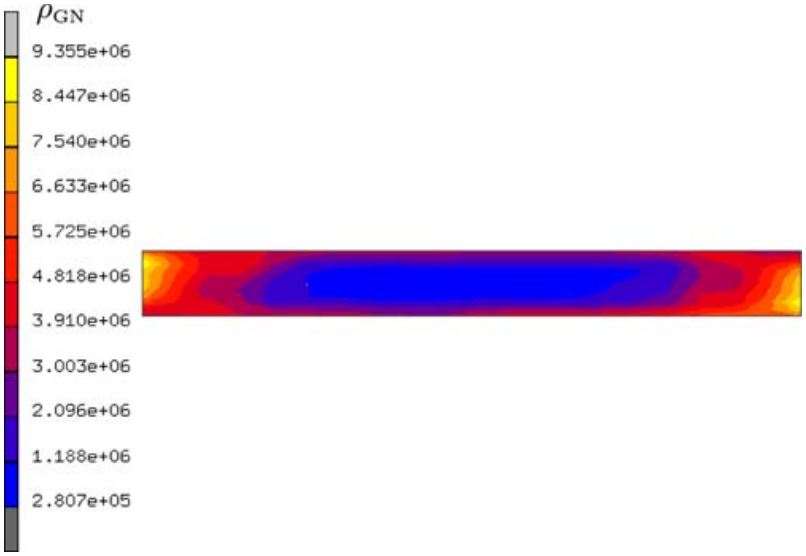

Fig. 6. Distribution of total geometrically necessary dislocation densities ρ_{GN} in 1/mm^2.

These figures clearly show the capability of the approach to describe size effects as with decreasing H the density of geometrically necessary dislocations increases yielding higher stresses through the height in the middle (horizontally, i.e. at $x = L/2$) of the laminate (Fig. 8) and higher stresses averaged over the laminate with decreasing heights (Fig. 9).

How strong the influence of the discretization actually is, can be seen in Fig. 10 where equivalent strain is plotted over the height for a structure with $H = 0.1$ mm. Note that the equivalent strain (which includes the elastic and the plastic strain components) at the boundary should be close to the elastic strain (as $\dot{\gamma} = 0$ is imposed at the boundary) which should be similar in all meshes. The reason for the differences lies in the data manipulation of the Finite Element software which projects the strains from the interior integration points to the boundary node. The influence of the meshes on the dislocation densities can be seen in Fig. 11 illustrating that quite a lot of elements have to be used through the height to obtain accurate dislocation densities and stresses as the stresses increase with the total dislocation density. In this respect it may be noted that elements with quadratic shape functions essentially deliver constant strain gradients within the element. A discretization with quadratic elements would therefore require the same mesh density as with the suggested approach while the numbers in nodes and bandwidth of the tangential stiffness matrix are far higher than with the suggested approach. Concerning the high values in ρ_{GN} in Fig. 11 in the finer meshes, it should be noted that zero slip is enforced at the top and bottom boundaries. Dislocations will therefore not be able to exit the material at the boundary and therefore accumulate. High dislocation densities should therefore be expected at the boundary. In assessing the absolute dislocation density values at these boundaries one has however to keep in mind that in the close neighborhood of the boundary micro-back stresses or other discrete dislocation forces may be present which are not reflected in the suggested material model. Such micro-forces would arguably result in a decrease in local dislocation densities.

As discussed in Section 3.1 the projection at the boundary nodes is not as good as in interior nodes. In this particular problem the gradients in the boundary elements have similar values as the neighboring elements to the inner part of the structure because the same patch node I_{patch} (Fig. 2) is used in the projection procedure. As gradients and the discretization

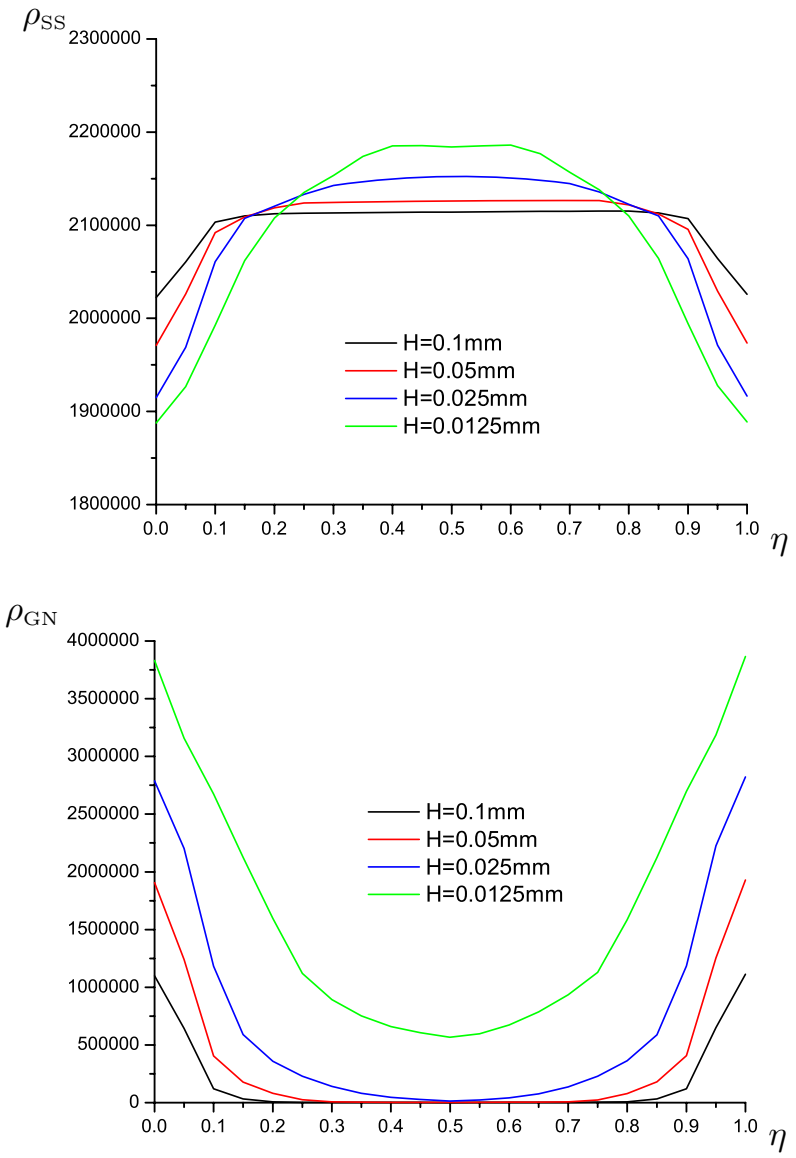

Fig. 7. ρ_{SS} and ρ_{GN} in $1/mm^2$ versus normalized vertical coordinate $\eta = y/H$ at $x = L/2$.

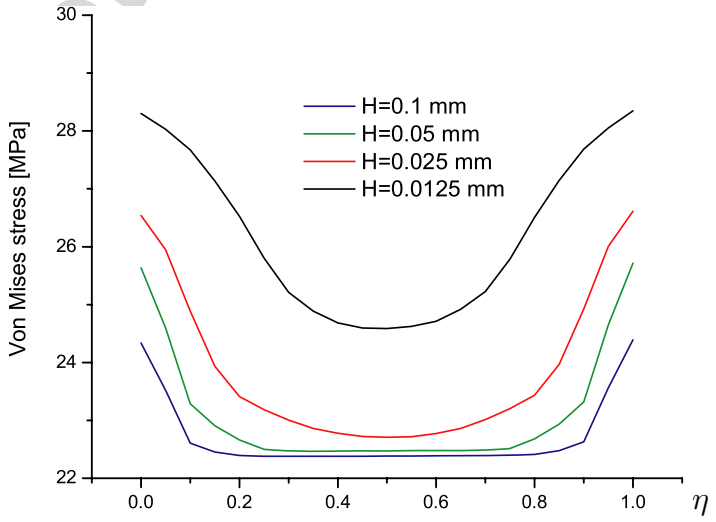

Fig. 8. Von Mises stresses (in MPa) versus versus normalized vertical coordinate $\eta = y/H$ at $x = L/2$.

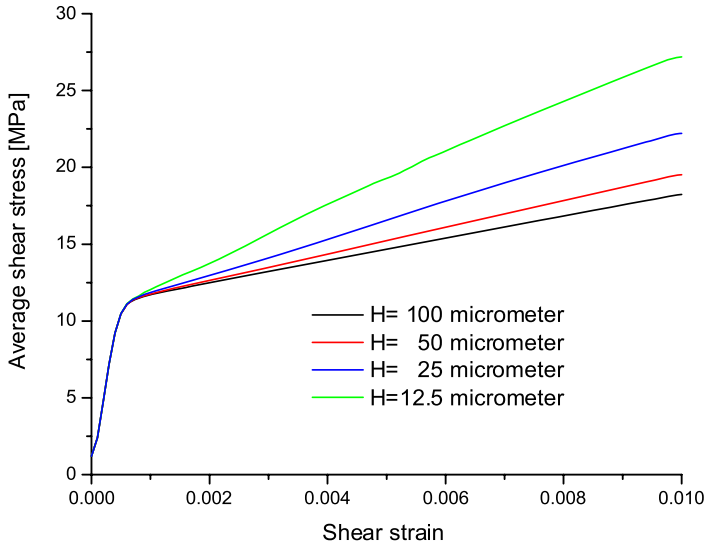

Fig. 9. Averaged shear stress versus shear strain.

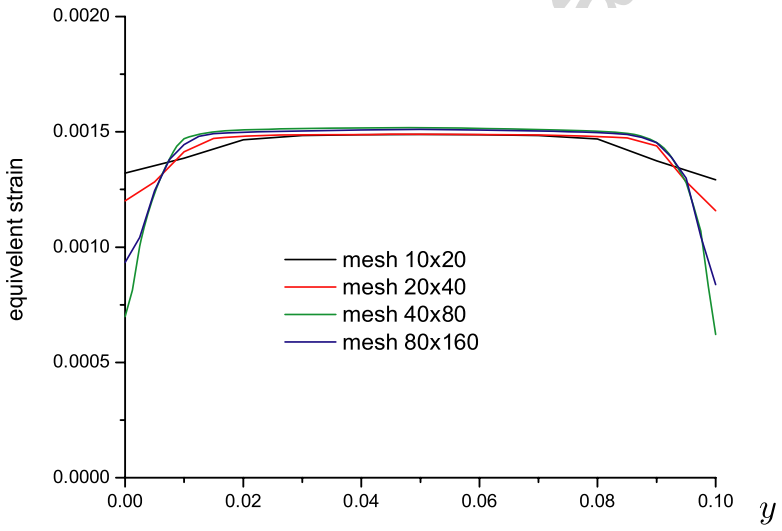

Fig. 10. Equivalent strain versus vertical coordinate y at $x = L/2$.

error at boundaries are in general higher than in the inner structure an adaptive discretization with smaller elements at the boundary and larger elements in the interior would have been computationally more advantageous. Particularly for strain gradient models as in this example, a computationally efficient procedure has therefore to be capable to discretize a structure non-uniformly which necessitates the capability to obtain strain gradient related terms within a non-uniform mesh. The patch recovery procedure (28)–(31) with the followed differentiation Eq. (32) provides such properties which directly follows from the obtained continuous $\boldsymbol{\Omega}$ field (see Zienkiewicz and Zhu, 1987, 1992a).

4.2. Indentation of a cylinder

In the second example a three dimensional indentation problem is considered. A non-uniform mesh is applied to demonstrate the capability of the approach for non-regular meshes. The mesh contains 7376 elements and 8680 nodes which is a rather rough discret-

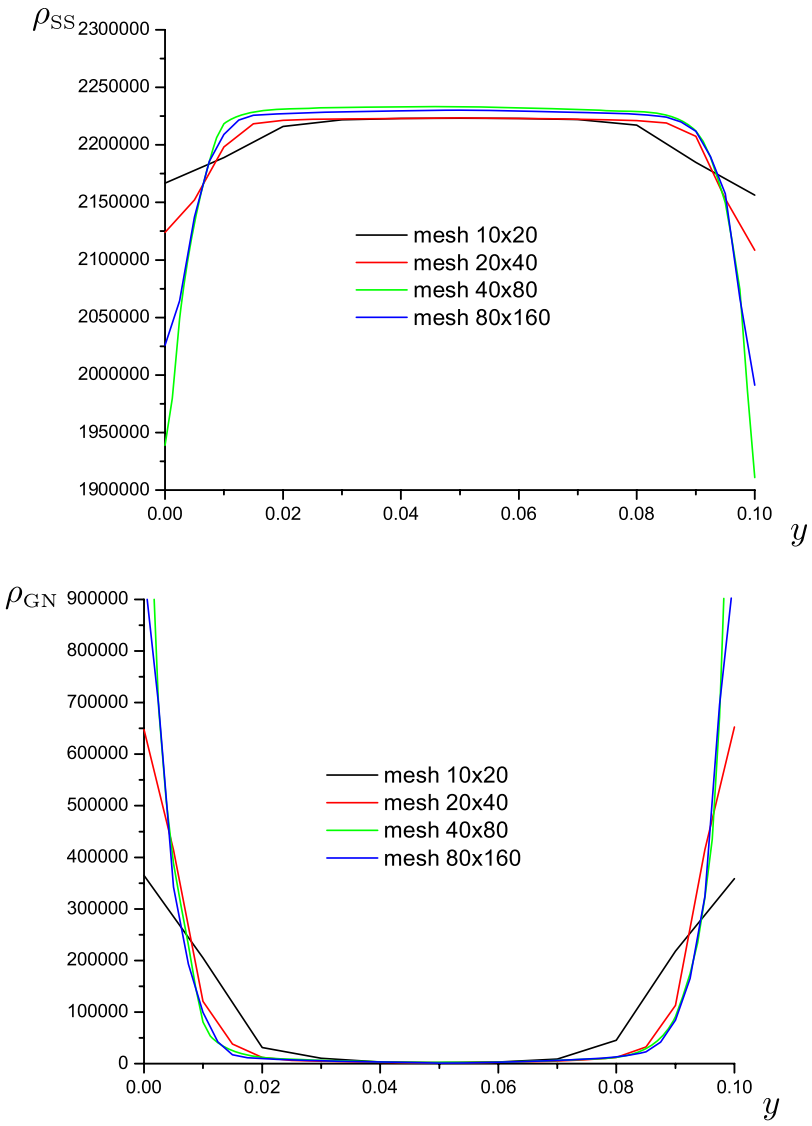

Fig. 11. ρ_{SS} and ρ_{GN} in 1/mm^2 versus vertical coordinate y in mm at $x = L/2$.

ization for this indentation problem. The discretization is denser in the upper middle area, where the rigid indenter deforms the structure, see Fig. 12, where the mesh of the undeformed cylinder is shown. A similar problem has also been studied applying an isotropic strain gradient plasticity model and a 2D axisymmetric discretization in Shu and Fleck (1998) and Qu et al. (2006). Comparisons with experiments of the in section two given materials formulation can be found in Ma et al. (2006) and Zaafarani et al. (2006). In Zaafarani et al. (2006) the here suggested numerical approach was actually applied without any description and discussions of the numerical approach itself.

The cylinder with height $h = 100$ μm and radius $r = 100$ μm is deformed by an indenter with a spherical tip with a radius of $R = 20$ μm. The simulation timeframe of 1000 s is subdivided into 200 time steps. Conventional Coulomb friction with a friction constant of 0.1 is applied. After first contact the indenter is vertically moved for 6 microns. The initial orientation of the crystal is chosen in such a way that the (1 1 1) is parallel to the vertical axis of the cylinder. The boundaries at the bottom of the cylinder are fixed in all directions. The contact forces of the indenter versus indentation depth of the simulation is given in Fig. 13.

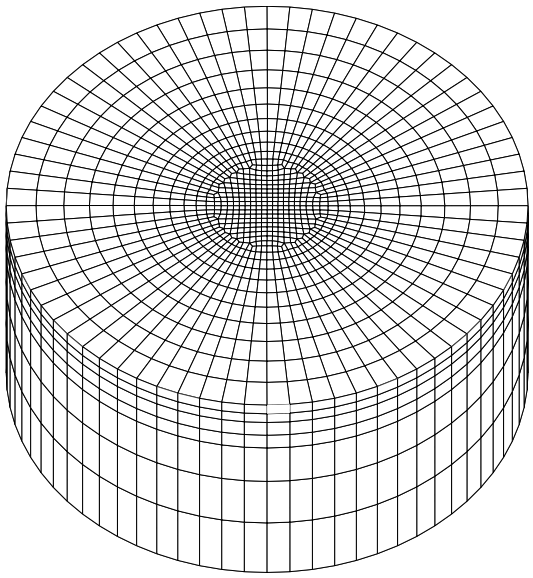

Fig. 12. Full Finite Element mesh of the undeformed cylinder.

Therein 'SSD' refers to the crystal plasticity model in Tables 2 and 3 where the influence of the density in the geometrically necessary dislocations is omitted and 'GND + SSD' to the full model described in Tables 2–4. With the loads of the 'GND + SSD' simulations being significantly higher than the load of 'SSD' this examples clearly exhibits a pronounced size effect often observed in experiments (see, e.g., Ma and Clarke, 1995).

In Fig. 14 the von Mises stresses in the deformed configuration are shown at an indentation depth of 5 μm where only the half of the cylinder is plotted. The stresses in the middle of the structure are more pronounced than on might expect for local isotropic materials. These high stresses can be partly attributed to the activation of more slip systems in the middle axis of the cylinder, see Fig. 15, which results in higher total dislocation density in the deformation process. As can be seen in the distribution of statistically stored dislocations densities, ρ_{SS}, in Figs. 16 and 17. Such an emphasis in the strains can not be observed, as the boundary conditions impede deformation particularly in the middle

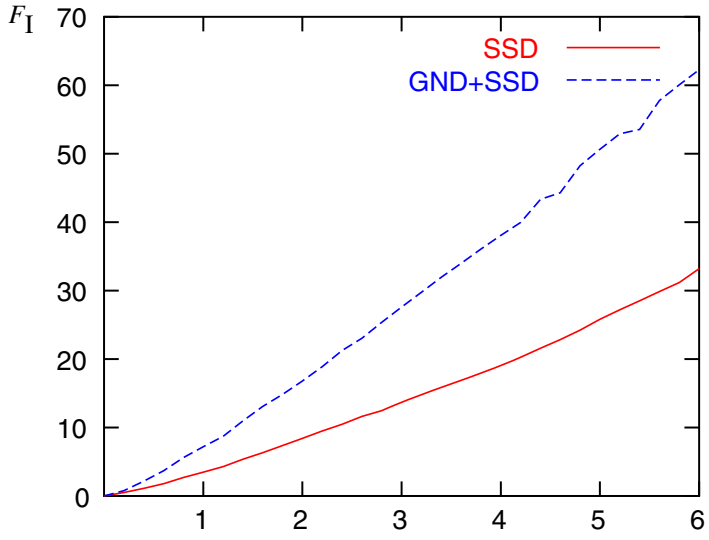

Fig. 13. Indenter force F_I in N versus indentation depth h in μm.

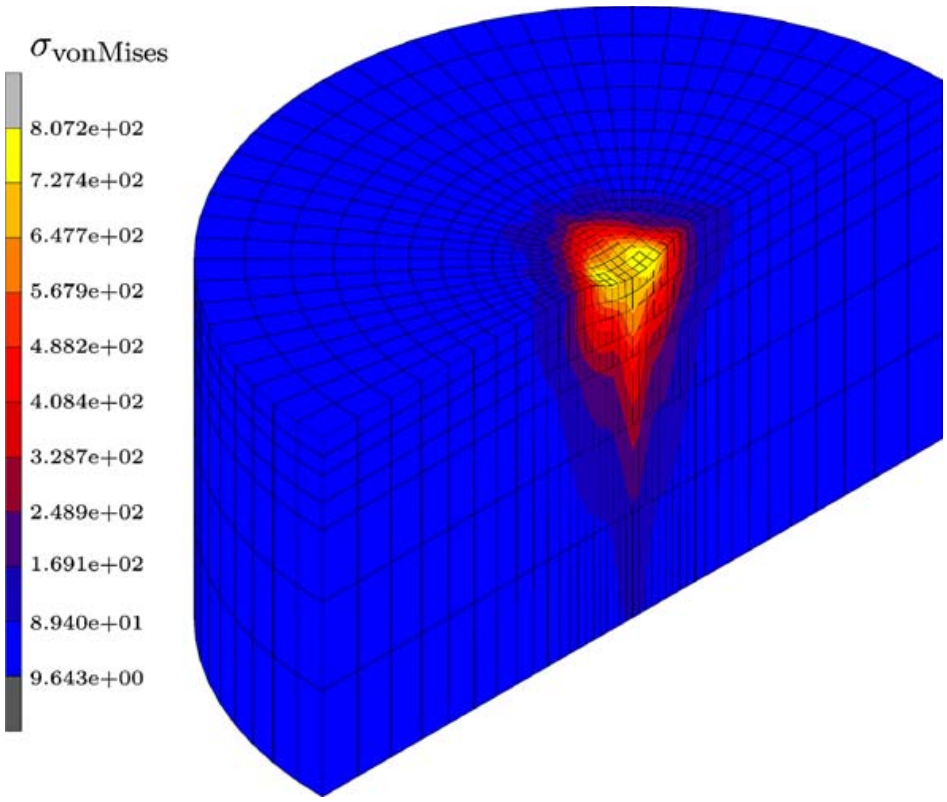

Fig. 14. Von Mises stresses $\sigma_{\text{von Mises}}$ in MPa.

where the vertical displacements is enforced at both ends so that the material can not move as easily as in other locations of the cylinder. The distribution in the equivalent strain with local values up to 0.31 is shown in Fig. 16.

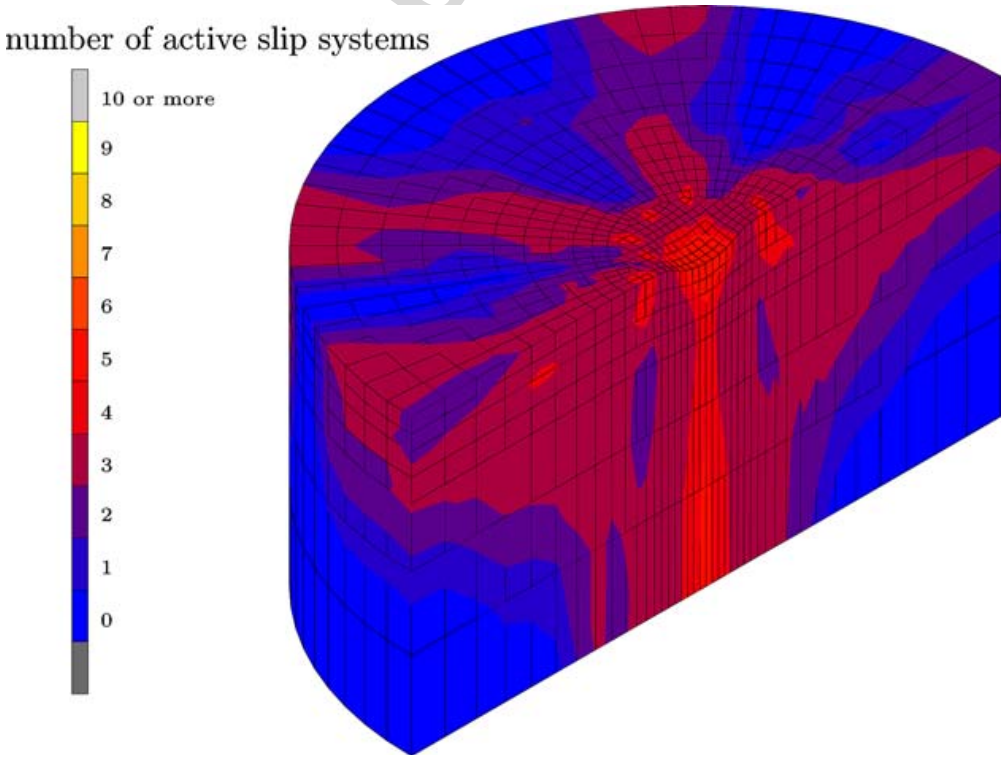

Fig. 15. Distribution of active slip systems.

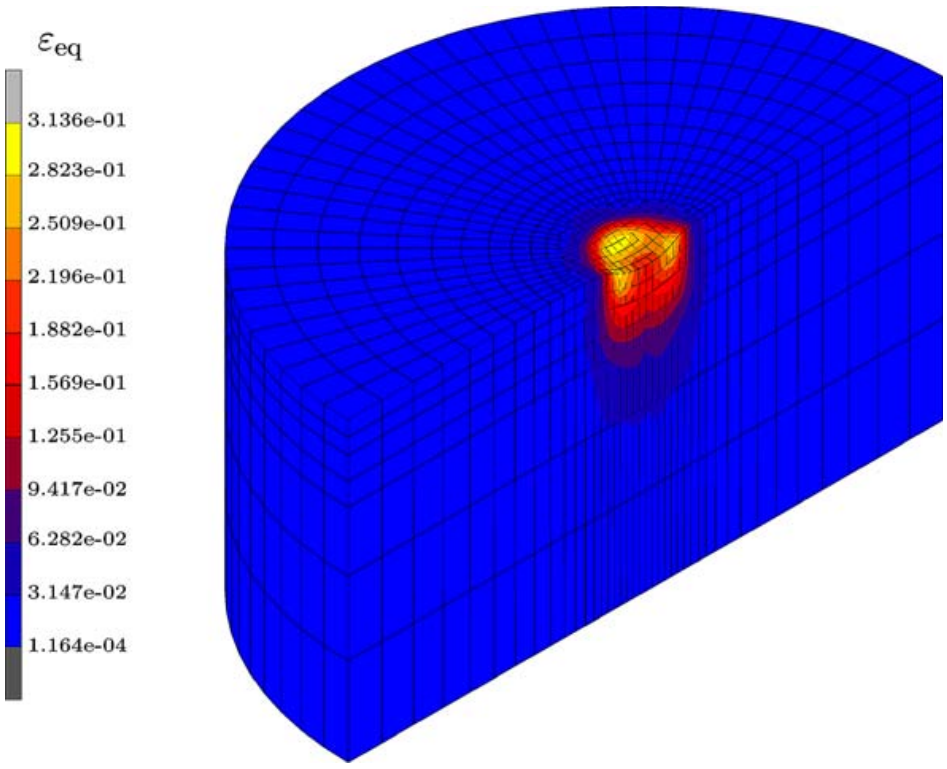

Fig. 16. Equivalent strains ε_{eq}.

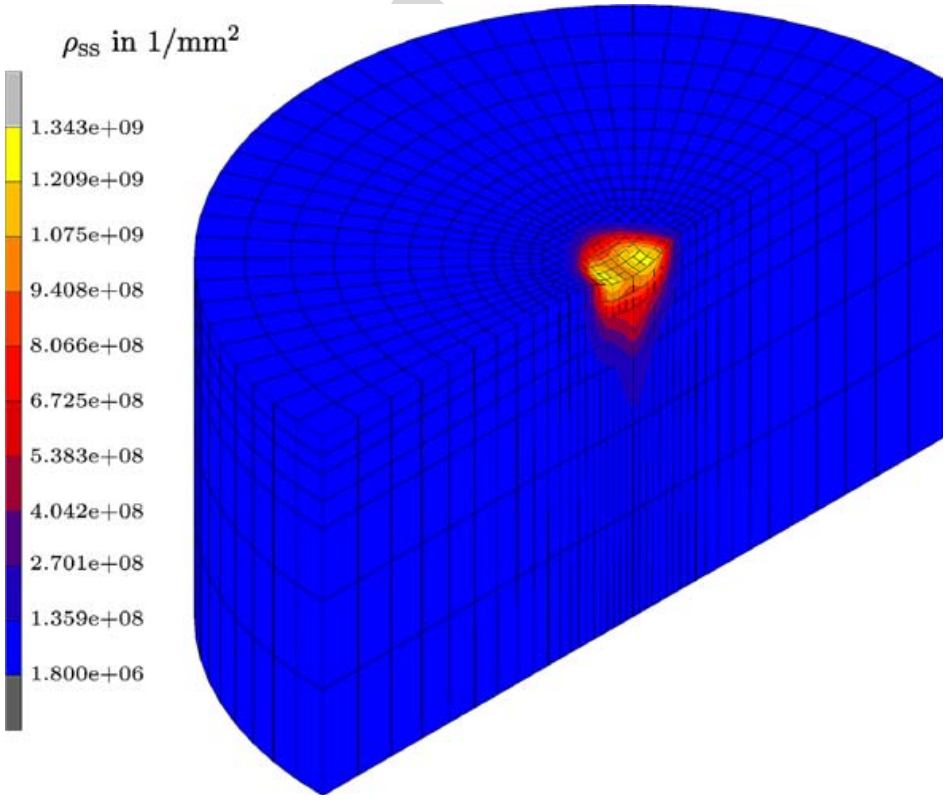

Fig. 17. Distribution of total statistically stored dislocation density ρ_{SS}.

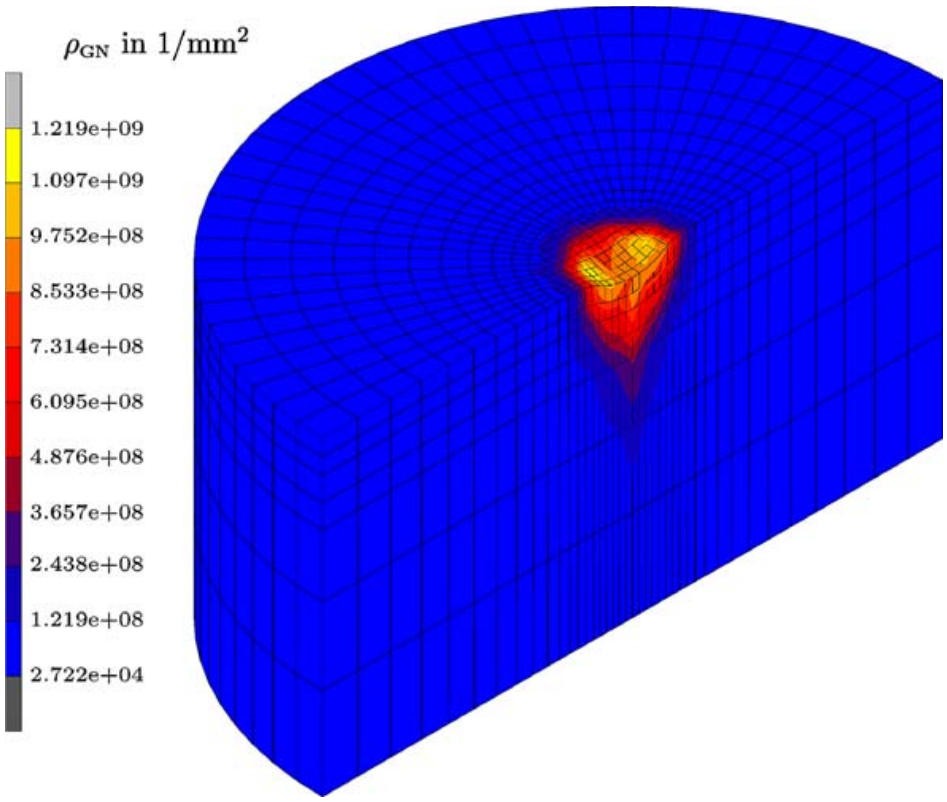

Fig. 18. Distribution of total geometrically necessary dislocation density ρ_{GN}.

The distribution of the total geometrically necessary dislocation densities, ρ_{GN}, shown in Fig. 18, may with respect to Fig. 16 appear not to be consistent in the context of the approximate rule that strain gradients scale proportional to the density of geometrically necessary dislocations ρ_{GN}. In strain gradient crystal plasticity the situation is however different as the activation of different slip systems can cause higher dislocation densities via local dislocation multiplication during the deformation process. In addition the cross-sectional plot of the strains in Fig. 16 can be somewhat misleading as there are lower gradients further away from the center axis of the cylinder because there will be only low gradients in the circumferential direction and most of gradients are of radial nature. In the center of the cylinder, however, gradients are present in three perpendicular directions yielding higher values if the norm of the strain gradient tensor or dislocation density tensor is evaluated. The range in ρ_{GN} is similar to those of the statistically stored dislocations and it might be worth noting that in the simulation where the geometrically necessary dislocations ρ_{GN} are omitted the calculated density in the statistically stored dislocations is with a range between $\rho_{SS} = 1.80 \times 10^6$–$6.27 \times 10^8 \frac{1}{mm^2}$ (not shown here) significantly lower than those with taking geometrically necessary dislocations ρ_{GN} into account ($\rho_{SS} = 1.80 \times 10^6$–$1.34 \times 10^9 \frac{1}{mm^2}$ in Fig. 17). The increase in ρ_{SS} clearly evolves from the interaction between ρ_{GN} via forest ρ_F^α, and parallel ρ_P^α and mobile dislocations ρ_M^α in Table 2 and 3.

5. Conclusions

A Finite Element technique with linear shape functions for non-local/gradient material formulation has been suggested. As linear shape functions yield basically a constant

distribution of strains and strain related terms the values of neighboring elements have to be used to obtain gradients in the strain. This is achieved here by applying the patch recovery technique known from error indication and adaptive meshing procedures also applicable to inhomogeneous Finite Element meshes. This procedure has been applied to a strain gradient crystal plasticity material formulation and the solution of this procedure requires an additional loop in the Newton–Raphson iteration scheme. The examples have shown that this procedure is capable in dealing with three dimensional large strain contact problems – indicating the robustness of the proposed approach – and yielded reasonable results. It should be noted that a solution of the three dimensional indentation with quadratic shape functions would have been computationally much more expensive. Generally the suggested procedure would also be applicable to other low order elements with linear shape functions, e.g. triangle or tetrahedron elements.

Acknowledgements

The support of this work by the North Dakota EPSCoR Program (EPS-0447679) and the EU FP6 Integrated Project IMPRESS (Contract NMP3-CT-2004-500635 – funding institutions: European Commission and European Space Agency) is highly appreciated.

References

Abu Al-Rub, R.K., Voyiadjis, G.Z., 2005. A direct finite element implementation of the gradient-dependent theory. Int. J. Num. Meth. Eng. 63, 603–629.

Abu Al-Rub, R.K., Voyiadjis, G.Z., 2006. A physically based gradient plasticity theory. Int. J. Plast. 22, 654–684.

Acharya, A., Bassani, J.L., 2000. Lattice incompatibility and a gradient theory of crystal plasticity. J. Mech. Phys. Sol. 48, 1565–1595.

Arsenlis, A., Parks, D.M., 1999. Crystallographic aspects of geometrically necessary and statistically stored dislocation density. Acta Mater. 47, 1597–1611.

Bittencourt, E., Needleman, A., Gurtin, M.E., van der Giessen, E., 2003. A comparison of nonlocal continuum and discrete dislocation plasticity predictions. J. Mech. Phys. Sol. 51, 281–310.

Boroomand, B., Zienkiewicz, O.C., 1997. An improved rep recovery and the effectivity robustness test. Int. J. Num. Meth. Eng. 40, 3247–3277.

Boroomand, B., Zienkiewicz, O.C., 1999. Recovery procedures in error estimation and adaptivity. Part II: Adaptivity in nonlinear problems of elasto-plasticity behaviour. Comp. Meth. Appl. Mech. Eng. 176, 127–146.

Cheong, K.S., Busso, E.P., Arsenlis, A., 2005. A study of microstructural length scale effects on the behaviour of fcc polycrystals using strain gradient concepts. Int. J. Plast. 21, 1797–1814.

Clayton, J.D., McDowell, D.L., Bammann, D.J., 2006. Modeling dislocations and disclinations with finite micropolar elastoplasticity. Int. J. Plast. 22, 210–256.

Cuitino, A.M., Ortiz, M., 1992. Computational modelling of single crystals. Modell. Simul. Mater. Sci. Eng. 1, 225–263.

Dai, H., Parks, D.M., 1997. Geometrically-necessary dislocation density and scale-dependent crystal plasticity. In: Khan, A. (Ed.), Proceedings of Sixth International Symposium on Plasticity, pp. 17–18.

Evers, L.P., Parks, D.M., Brekelmans, W.A.M., Geers, M.G.D., 2002. Crystal plasticity model with enhanced hardening by geometrically necessary dislocation accumulation. J. Mech. Phys. Sol. 50, 2403–2424.

Fleck, N.A., Hutchinson, J.W., 1997. Strain gradient plasticity. Adv. Appl. Mech. 33, 295–361.

Fleck, N.A., Muller, G.M., Ashby, M.F., Hutchinson, J.W., 1994. Strain gradient plasticity: theory and experiment. Acta Metal. Mater. 42, 475–487.

Gao, H., Huang, Y., Nix, W.D., Hutchinson, J.W., 1999. Mechanism-based strain gradient plasticity – I. Theory. J. Mech. Phys. Sol. 47, 1239–1263.

Han, C.-S., Wriggers, P., 2000. An h-adaptive method for elasto–plastic shell problems. Comp. Meth. Appl. Mech. Eng. 189, 651–671.

Han, C.-S., Wriggers, P., 2002. On the error indication of shells in frictionless unilateral contact. Comput. Mech. 28, 169–176.
Han, C.-S., Wagoner, R.H., Barlat, F., 2004. On precipitate induced hardening in crystal plasticity: algorithms and simulations. Int. J. Plast. 20, 1441–1461.
Han, C.-S., Gao, H., Huang, Y., Nix, W.D., 2005a. Mechanism-based strain gradient crystal plasticity – I. Theory. J. Mech. Phys. Solids 53, 1188–1203.
Han, C.-S., Gao, H., Huang, Y., Nix, W.D., 2005b. Mechanism-based strain gradient crystal plasticity – II. Analysis. J. Mech. Phys. Solids 53, 1204–1222.
Han, C.-S., Hartmaier, A., Gao, H., Huang, Y., 2006. Discrete dislocation dynamics simulations of surface induced size effects in plasticity. Mater. Sci. Eng. A 415, 225–233.
Huang, Y., Gao, H., Nix, W.D., Hutchinson, J.W., 2000. Mechanism-based strain gradient plasticity – II. Analysis. J. Mech. Phys. Sol. 48, 99–128.
Huang, Y., Qu, S., Hwang, K.C., Li, M., Gao, H., 2004. A conventional theory of mechanism-based strain gradient plasticity. Int. J. Plast. 20, 753–782.
Kalidindi, S.R., Anand, L., 1992. Approximate procedure for predicting the evolution of crystallographic texture in bulk deformation processing of fcc metals. Int. J. Mech. Sci. 34, 309–329.
Liebe, T., Steinmann, P., 2001. Theory and numerics of a thermodynamically consistent framework for geometrically linear gradient plasticity. Int. J. Num. Meth. Eng. 51, 1437–1467.
Ma, Q., Clarke, D.R., 1995. Size dependent hardness of silver single crystals. J. Mater. Res. 10, 853–863.
Ma, A., Roters, F., 2004. A constitutive model for fcc single crystals based on dislocation densities and its application to uniaxial compression of aluminum single crystals. Acta Mater. 52, 3603–3612.
Ma, A., Roters, F., Raabe, D., 2006. A dislocation density based constitutive model for crystal plasticity FEM including geometrically necessary dislocations. Acta Mater. 54, 2169–2179.
Meissonnier, F.T., Busso, E.P., O'Dowd, N.P., 2001. Finite element implementation of a generalised non-local rate-dependent crystallographic formulation for finite strains. Int. J. Plast. 17, 601–640.
Menzel, A., Steinmann, P., 2000. On the continuum formulation of higher gradient plasticity for single and polycrystals. J. Mech. Phys. Sol. 48, 1777–1796.
Mesarovic, S. Dj., 2005. Energy, configurational forces and characteristic lengths associated with the continuum description of geometrically necessary dislocations. Int. J. Plast. 21, 1855–1889.
Miehe, C., Schröder, J., 2001. A comparative study of stress update algorithms for rate-independent and rate-dependent crystal plasticity. Int. J. Num. Meth. Eng. 50, 273–298.
Niordson, C.F., Hutchinson, J.W., 2003. Non-uniform plastic deformation of micron scale objects. Int. J. Num. Meth. Eng. 56, 961–975.
Nye, J.F., 1953. Some geometrical relations in dislocated solids. Acta Metal. 1, 153–162.
Ohashi, T., 1997. Finite-Element analysis of plastic slip and evolution of geometrically necessary dislocations in fcc crystals. Phil. Mag. Lett. 75, 51–57.
Ohashi, T., 2004. Three dimensional structures of the geometrically necessary dislocations in matrixinclusion systems under uniaxial tensile loading. Int. J. Plast. 20, 1093–1109.
Ohashi, T., 2005. Crystal plasticity analysis of dislocation emission from micro voids. Int. J. Plast. 21, 2071–2088.
Qu, S., Huang, Y., Pharr, G.M., Hwang, K.C., 2006. The indentation size effect in the spherical indentation of iridium: A study via the conventional theory of mechanism-based strain gradient plasticity. Int. J. Plast. 22, 1265–1286.
Rieger, A., Wriggers, P., 2004. Adaptive methods for thermomechanical coupled contact problems. Int. J. Num. Meth. Eng. 59, 871–894.
Roters, F., 2003. A new concept for the calculation of the mobile dislocation density in constitutive models of strain hardening. Phys. Stat. Sol. B 240, 68–74.
Shu, J.Y., Fleck, N.A., 1998. The prediction of a size effect in micro-indentation. Int. J. Sol. Struct. 35, 1363–1383.
Shu, J.Y., King, W.E., Fleck, N.A., 1999. Finite elements for materials with strain gradient effects. Int. J. Num. Mech. Eng. 44, 373–391.
Soh, A.-K., Wangji, C., 2004. Finite element formulations of strain gradient theory for microstructures and the C^{0-1} patch test. Int. J. Num. Meth. Eng. 61, 433–454.
Wang, Y., Raabe, D., Klüber, C., Roters, F., 2004. Orientation dependence of nanoindentation pile-up patterns and of nanoindentation microtextures in copper single crystals. Acta Mater. 52, 2229–2238.
Wiberg, N.-E., Abdulwahab, F., Ziukas, S., 1994. Enhanced superconvergent patch recovery incorporating equilibrium and boundary conditions. Int. J. Num. Meth. Eng. 36, 3417–3440.

Wriggers, P., 2001. Nichtlineare Finite-Element-Methoden. Springer.
Yefimov, S., Groma, I., van der Giessen, E., 2004. A comparison of a statistical-mechanics based plasticity model with discrete dislocation plasticity calculations. J. Mech. Phys. Sol. 52, 279–300.
Zaafarani, N., Raabe, D., Singh, R.N., Roters, F., Zaefferer, S., 2006. Three dimensional investigation of the texture and microstructure below a nanoindent in a cu single crystal using 3D EBSD and crystal plasticity Finite Element simulations. Acta Mater. 54, 1863–1876.
Zienkiewicz, O.C., Zhu, J.Z., 1987. A simple error estimator and adaptive procedures for practical engineering analysis. Int. J. Num. Meth. Eng. 24, 337–357.
Zienkiewicz, O.C., Zhu, J.Z., 1992a. The superconvergent patch recovery and a posteriori error estimates. Part 1: the recovery technique. Int. J. Num. Meth. Eng. 33, 1331–1364.
Zienkiewicz, O.C., Zhu, J.Z., 1992b. The superconvergent patch recovery and a posteriori error estimates. Part 2: error estimates and adaptivity. Int. J. Num. Meth. Eng. 33, 1365–1382.